A case study of the radiative forcing of persistent contrails evolving into contrail-induced cirrus

James M. Haywood,[1] Richard P. Allan,[2] Jorge Bornemann,[1] Piers M. Forster,[3] Peter N. Francis,[1] Sean Milton,[1] Gaby Rädel,[4] Alexandru Rap,[3] Keith P. Shine,[4] and Robert Thorpe[1]

[1] The radiative forcing due to a distinct pattern of persistent contrails that form into contrail-induced cirrus near and over the UK is investigated in detail for a single case study during March 2009. The development of the contrail-induced cirrus is tracked using a number of high-resolution polar orbiting and lower-resolution geostationary satellite instruments and is found to persist for a period of around 18 h, and at its peak, it covers over 50,000 km^2. The shortwave (SW) and longwave (LW) radiative forcing of the contrail-induced cirrus is estimated using a combination of geostationary satellite instruments, numerical weather prediction models, and surface observation sites. As expected, the net radiative effect is a relatively small residual of the much stronger but opposing SW and LW effects, locally totaling around 10 W m^{-2} during daylight hours and 30 W m^{-2} during nighttime. A simple estimate indicates that this single localized event may have generated a global-mean radiative forcing of around 7% of recent estimates of the persistent contrail radiative forcing due to the entire global aircraft fleet on a diurnally averaged basis. A single aircraft operating in conditions favorable for persistent contrail formation appears to exert a contrail-induced radiative forcing some 5000 times greater (in W m^{-2} km^{-1}) than recent estimates of the average persistent contrail radiative forcing from the entire civil aviation fleet. This study emphasizes the need to establish whether similar events are common or highly unusual for a confident assessment of the total climate effect of aviation to be made.

1. Introduction

[2] The rapid growth and the forecast future expansion of the aviation industry mean that the potential climatic effects have received considerable attention over the past decade [e.g., *Intergovernmental Panel on Climate Change* (*IPCC*), 1999; *Sausen et al.*, 2005; *Lee et al.*, 2009]. The civil aviation industry currently emits around 2–3% of all carbon dioxide emissions on a global basis, but the total impact upon the Earth radiation budget is thought to be higher primarily because of the radiative impact of persistent condensation trails (contrails) and aviation-induced cirrus. Aviation-induced cirrus can occur through two different pathways: via contrails spreading out and by injection of aerosols into the upper troposphere to provide ice nuclei that may subsequently form cirrus clouds [*Lee et al.*, 2009]. Our

study is restricted to the first of these, and we therefore refer to contrail-induced cirrus throughout this work. Contrails may form when emissions of hot, warm engine exhaust in the upper troposphere mix with the cool moist ambient atmosphere. Under certain atmospheric conditions (supersaturated with respect to ice), contrails can persist for several hours. If the atmospheric conditions are favorable for ice crystal growth these persistent contrails may grow and spread out to form contrail-induced cirrus clouds [e.g., *Fahey et al.*, 1999]. Persistent contrails and contrail-induced cirrus exert a radiative forcing in both the shortwave (SW) solar spectrum and longwave (LW) terrestrial spectrum [e.g., *Stuber et al.*, 2006; *Kärcher and Spichtinger*, 2009]. They reflect incident sunlight back to space thereby brightening the planet and leading to a negative SW radiative forcing that is associated with a cooling. They also trap LW radiation within the Earth atmosphere system leading to a positive LW radiative forcing that is associated with a warming. The net radiative effect of persistent contrails and contrail-induced cirrus is the sum of the negative SW radiative forcing and positive LW radiative forcing, resulting in a net forcing that is believed to be positive but rather

[1]Forecasting Research and Development, Met Office, Exeter, UK.
[2]ESSC, University of Reading, Reading, UK.
[3]Department of Environmental Science, University of Leeds, Leeds, UK.
[4]Department of Meteorology, University of Reading, Reading, UK.

small in magnitude [e.g., *Myhre and Stordal*, 2001, *Stuber et al.*, 2006, *Rädel and Shine*, 2008].

[3] The earliest comprehensive estimate of the impact of aviation emissions for aircraft operations in 1992 [*Prather et al.*, 1999; *IPCC*, 1999] suggested a radiative forcing of 20 mW m^{-2} for the formation of persistent contrails with considerable uncertainty. The estimate of the radiative forcing from contrail-induced cirrus was thought to be so uncertain that it could not even be quantified. The radiative forcing of persistent contrails and contrail-induced cirrus has been estimated in more recent studies at 10 mW m^{-2} by *Sausen et al.* [2005] and 30 mW m^{-2} (range 10–80 mW m^{-2}) by *Stordal et al.* [2005], respectively. This assessment of persistent contrails was adopted by *Forster et al.* [2007] and *IPCC* [2007] who assigned a 90% confidence interval of 6–30 mW m^{-2}. *Forster et al.* [2007] also point out the inherent ambiguity in trying to determine and separate aviation-induced cloudiness from persistent line-shaped contrails: the line-shaped contrails typically shear and spread and lose their characteristic shape while evolving into contrail-induced cirrus [e.g., *Minnis et al.*, 1998]. Thus, estimates of the ratio of the RF from contrail-induced cirrus to persistent contrails are highly uncertain and range from about 1 to 8 [e.g., *Lee et al.*, 2009]. These estimates of the radiative forcing of contrail-induced cirrus typically are derived from satellite retrievals by considering the spatial correlation of the radiances in water vapor, infrared, and/or solar channels with aviation traffic routes and by applying suitable threshold criteria [e.g., *Minnis et al.*, 1998, 2004; *Mannstein and Schumann*, 2005], but the difficulties in distinguishing contrail-induced cirrus from natural cirrus are severe [*Mannstein and Schumann*, 2007].

[4] The uncertainty in estimates of the radiative forcing of persistent linear contrails and the evolution into contrail-induced cirrus means that observational case studies are necessary to better understand their physical and radiative properties. *Minnis et al.* [1998] used geostationary satellite instruments to track distinctly shaped contrails evolving into cirrus in three separate events during April–May 1996 and detailed the microphysical evolution of the cirrus particles together with the cirrus optical depth cloud top temperature and area extent. Essentially, we perform a similar study but use polar orbiting satellite data that are available at higher frequency nowadays to track the evolution of a characteristic contrail shape as it evolved into cirrus. We extend the approach of *Minnis et al.* [1998] by utilizing surface and satellite measurements in conjunction with operational numerical weather prediction (NWP) models to isolate both the SW and LW RF of the contrail-induced cirrus. Unlike other studies (e.g., A. Rap et al., Parameterization of contrails in the UK Met Office Climate Model, submitted to *Journal of Geophysical Research*, 2009), our methodology does not rely on explicit modeling of the persistent contrails and contrail-induced cirrus themselves. The radiative forcing is deduced by subtracting the irradiances from satellite observations of contrail-induced cirrus from the irradiances derived from the NWP model which does not include contrails.

[5] A distinct coil-shaped contrail evolving into cirrus (hereafter CCC) that is thought to have originated from maneuvers performed by an Airborne Warning and Control System (AWACS) aircraft was observed in satellite imagery

during March 2009 (Figure 1). Figure 1 (left) shows that the CCC is difficult to detect in visible imagery owing to the presence of extensive stratocumulus cloud at lower levels. Indeed the shadow of the contrail on the lower stratocumulus clouds, which causes a reduction in reflectance, is more readily detectable than any increase in reflectance. Figure 1 (right) shows that the CCC is, however, very readily discernable in the infrared wavelengths because of the large difference in the emission temperature between the CCC and the low-level stratocumulus. Both images show that while the CCC is by far the most distinguishable contrail occurring over the North Sea, several other contrails are also visible off the coast of Scotland and England and encroach over southeast England.

[6] In this study we analyze the meteorological conditions which are shown to favor persistent contrail formation between approximately 25,000–35,000 ft (1 ft = 0.3048 m) (7.5 to 10.5 km) (section 2). Polar orbiting satellite instruments that detect cloud at infrared (10.8 μm) wavelengths are used to record the evolution of the CCC over a 10 h period and an atmospheric dispersion model is used to verify the position of the coil-shaped contrail as it shears and spreads (section 3). The study also uses independent measurements from the geostationary Meteosat-9 satellite Spinning Enhanced Visible and InfraRed Imager (SEVIRI) instrument to track the CCC and other persistent contrails as they advect and evolve. Although analysis of the evolution of ice crystal effective radius and cirrus optical depth are hampered by the presence of low-level stratocumulus and the advection over variable land surfaces, retrievals are possible over ocean surfaces free from low-level cloud (section 4). The advection of the contrail-induced cirrus over land means that instrumented meteorological observation sites may also be used to determine the SW radiative forcing at the surface (section 5). The SW and the LW top of the atmosphere radiative forcings are estimated by comparing the SW and LW irradiances derived from the Met Office high-resolution (4 km) UK4 operational NWP model (section 6). A discussion and conclusion are then provided (section 7).

2. Prevailing Meteorological Conditions

[7] The synoptic surface analysis chart for 1200 (all times refer to UTC) on 20 March 2009 is shown in Figure 2. A large anticyclone is centered on the United Kingdom with a central surface pressure of around 1034–1035 hPa. The United Kingdom is in a stable warm sector with a weak frontal system approaching only very slowly from the west. The small pressure gradients mean that wind is slack across the United Kingdom. Figure 3 shows the tephigrams derived from radiosonde ascents from Met Office sites for 1200 UTC for Nottingham (53.00°N, 1.25°W), Albermarle (55.01°N, 1.52°W), and Ekofisk (56.53°N, 3.21°E) (see geographical positions marked on Figure 1). *Rädel and Shine* [2007] have shown that provided corrections are made to the relative humidity derived from these sondes, they can be used quite reliably to infer conditions necessary for the formation of persistent contrails. All three of the tephigrams show a strong subsidence temperature inversion indicating highly stable atmospheric conditions to around 900 hPa. At low levels the atmosphere is
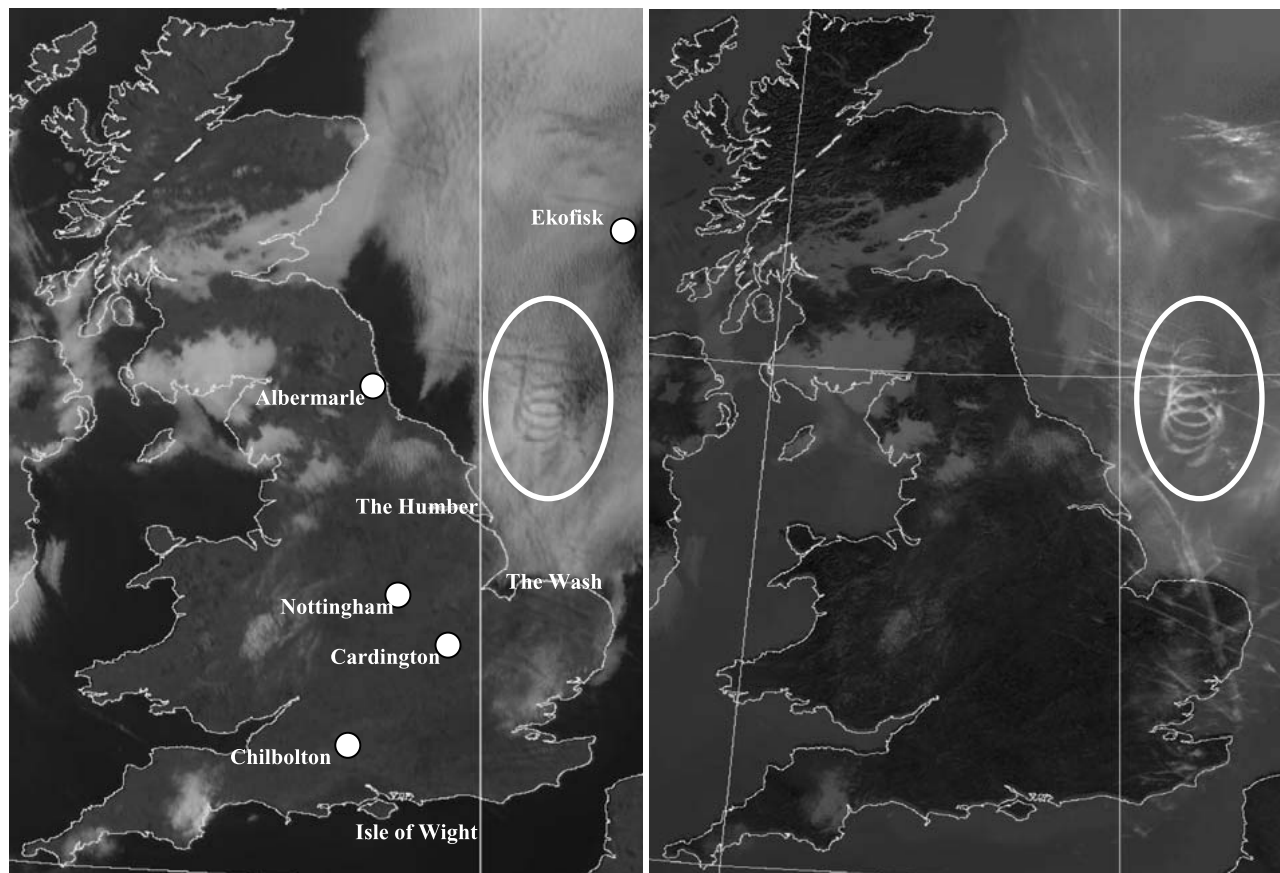
Figure 1. (left) High-resolution visible image (0.65 μm) from the SEVIRI sensor on Meteosat-9. (right) Infrared (10.8 μm) image obtained from the METOP satellite. Both images are from ∼1040 UTC on 20 March 2009. The white oval highlights the position of the coil-shaped contrail/cirrus (CCC). The positions of the World Meteorological Organization radiosonde ascent sites at Nottingham, Albermarle, and Ekofisk are also shown together with the approximate position of the Met Office Cardington field site and the Chilbolton observatory.

Figure 2. The synoptic surface analysis from the UK Met Office for 1200 UTC on 20 March 2009.
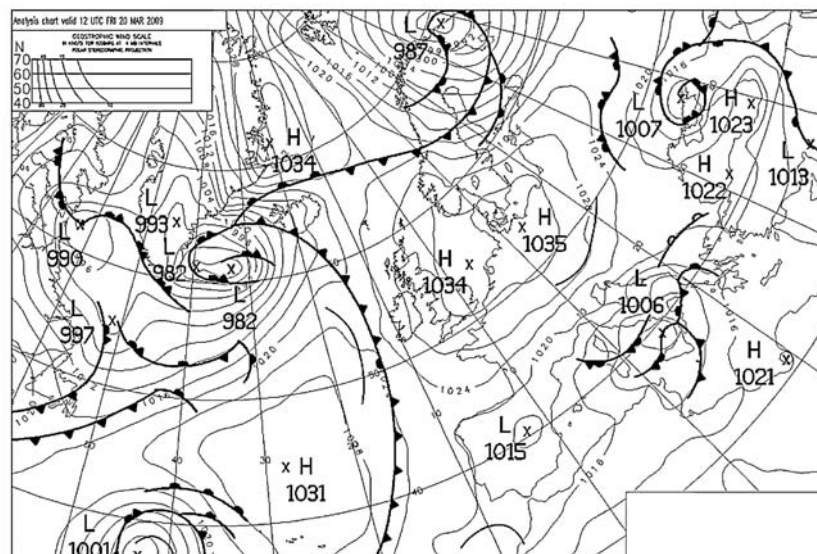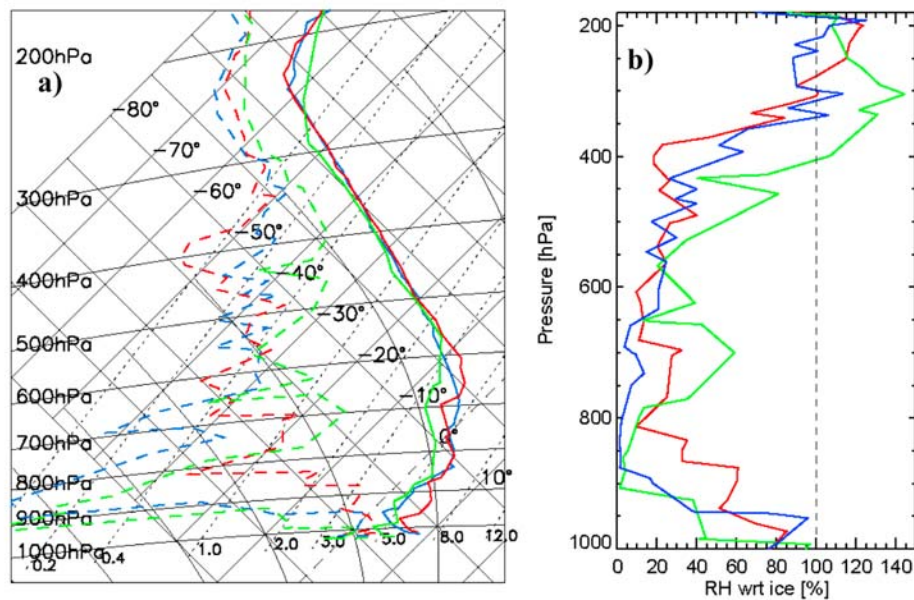
Figure 3. Tephigrams showing (a) the radiosonde ascent profiles of temperature and dew point from Nottingham (blue), Albemarle (red), and Ekofisk (green) for 1200 UTC on 20 March 2009, (b) the relative humidity with respect to ice determined from the tephigrams is shown in Figure 2b derived using the correction of *Vömel et al.* [2007].

dry with water vapor mass mixing ratios lower than 0.2–0.4 g kg^{-1} evident in the Nottingham and Ekofisk ascents. The lack of moisture in the atmospheric column is reflected by the low total precipitable water values of 5.2, 8.5, and 6.7 cm for the Nottingham, Albermarle, and Ekofisk ascents, respectively. At upper levels, the Ekofisk sounding shows a similar temperature profile to the other two radiosonde ascents, but the water vapor mass mixing ratio is significantly higher between 250 and 500 hPa indicating a moister upper troposphere. The relative humidity with respect to ice calculated from the profiles making the corrections to relative humidity recommended by *Rädel and Shine* [2007] based on *Vömel et al.* [2007] is shown in Figure 3b. At upper levels, the relative humidity only very slightly exceeds 100% for Nottingham but exceeds 100% for Albermarle above about 275 hPa. For the Ekofisk ascent a much greater altitude range (200–400 hPa) is subject to ice supersaturation conditions meaning that persistent contrail formation and growth may therefore be expected near the Ekofisk oil platform provided that the ambient temperature is below the minimum temperature for contrail formation: the Ekofisk tephigrams reveals a temperature at 300 hPa of around −50°C which is sufficient for contrail initiation. Thus, one might expect contrails to be initiated and spread around the Ekofisk region of the North Sea. This is consistent with visual inspection of the contrails shown in Figure 1.

[8] Inspection of fields of the relative humidity with respect to ice from the operational UK4 model reveals that, although the relative humidity with respect to ice frequently approaches 100%, no areas of supersaturation are found over the North Sea between pressure levels of 300–350 hPa over the period 1200 UTC on 20 March 2009 to 0000 UTC on 21 March 2009. In common with many of the current

Met Office Numerical Weather Prediction models [e.g., *Newman et al.*, 2008] and the climate model (A. Rap et al., submitted manuscript, 2009), this deficiency in model performance appears to be linked to too dry a modeled upper troposphere. Not all operational NWP models exhibit this deficiency. Figure 4a shows the relative humidity with respect to ice determined from a 12 h forecast of European Centre for Medium-Range Weather Forecasts (ECMWF) operational model. The forecast relative humidity over the North Sea at 1200 UTC is seen to exceed 100% between levels of 25,000–35,000 ft (7.5–10.5 km), with peak values exceeding 130% above 32,500 ft (∼9.7 km). Figure 4b shows the evolution of the ice-supersaturated region at 30,500 ft (9.2 km). The region of ice supersaturation is seen to persist throughout the period shown and drift southward with the prevailing winds shown in Figure 4a.

[9] Further efforts are obviously needed to improve the Met Office suite of models in terms of their upper tropospheric moisture, particularly if the Met Office is to improve its contrail forecasting capability from the model. However, here we turn this deficit to our advantage; because the model does not predict any significant ice supersaturation and hence no upper level cirrus, the difference between the modeled and observed radiative fluxes at the top of the atmosphere are essentially equivalent to the radiative forcing of the contrails/cirrus. This methodology assumes that the radiative effect of the moisture deficit is second order compared to the radiative effect of the contrails, which radiative transfer calculations show to be a reasonable assumption. Such an approach has previously been used for determining the radiative effects of mineral dust over the Sahara desert [*Haywood et al.*, 2005]. One particularly significant advantage of this approach is that it does not rely to any degree on accurate modeling of the detailed microphysics and spatial distribution of the contrails/cirrus;
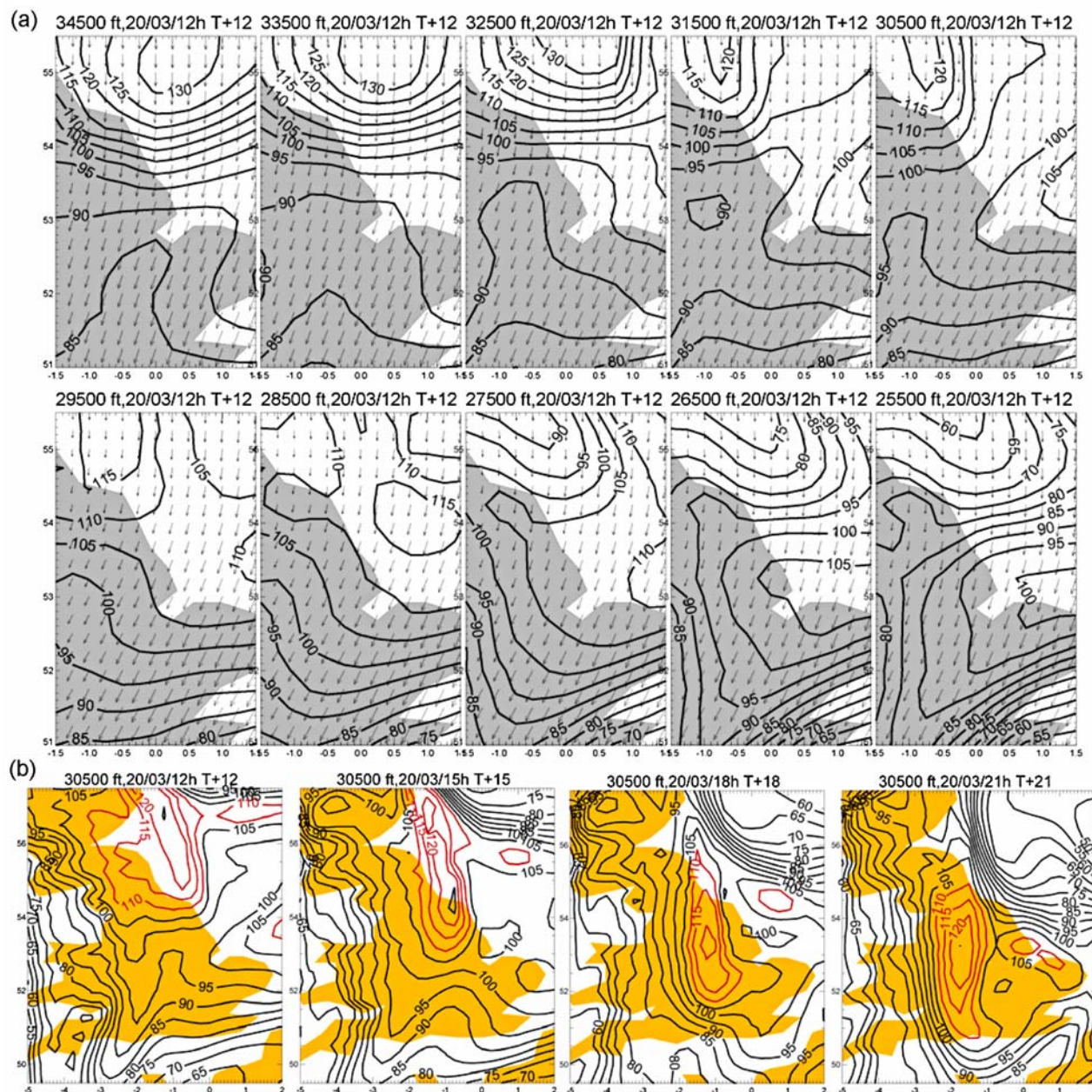
Figure 4. Showing the relative humidity with respect to ice over the United Kingdom derived from the ECMWF operational model. (a) Altitudes from 34,500 ft (top left) to 25,500 ft (bottom right) and model levels every 1000 ft in between. The contours show relative humidity (%), and the arrows represent wind vectors. Fields are for 1200 UTC on 20 March 2009 from forecasts at 0000 UTC on 20 March 2009. (b) The evolution of the supersaturated region at 30,500 ft over the period 1200–2100 UTC. Regions with relative humidity exceeding 110% with respect to ice are contoured in red.

only radiative transfer in the absence of contrails/cirrus needs to be performed. This methodology will be considered in more detail in section 6.

3. Evolution of the Contrails Into Cirrus

[10] As shown in Figure 1, the CCC is most readily distinguished from the low-level stratocumulus cloud using infrared (10.8 μm) wavelengths. Figure 5 shows the evolution of fresh, linear contrails and the CCC.

[11] The majority of the fresh, relatively narrow, linear contrails appear to be initiated between about 0830 and 1200 UTC. The satellite imagery suggests that prior to around 1200 UTC, the majority of contrails that are growing into contrail-induced cirrus appear to be initiated over the North Sea although a few also appear over the southeast of the United Kingdom. After 1200 UTC the area of contrail-induced cirrus is advected over land areas of the United Kingdom which is in reasonable agreement with the
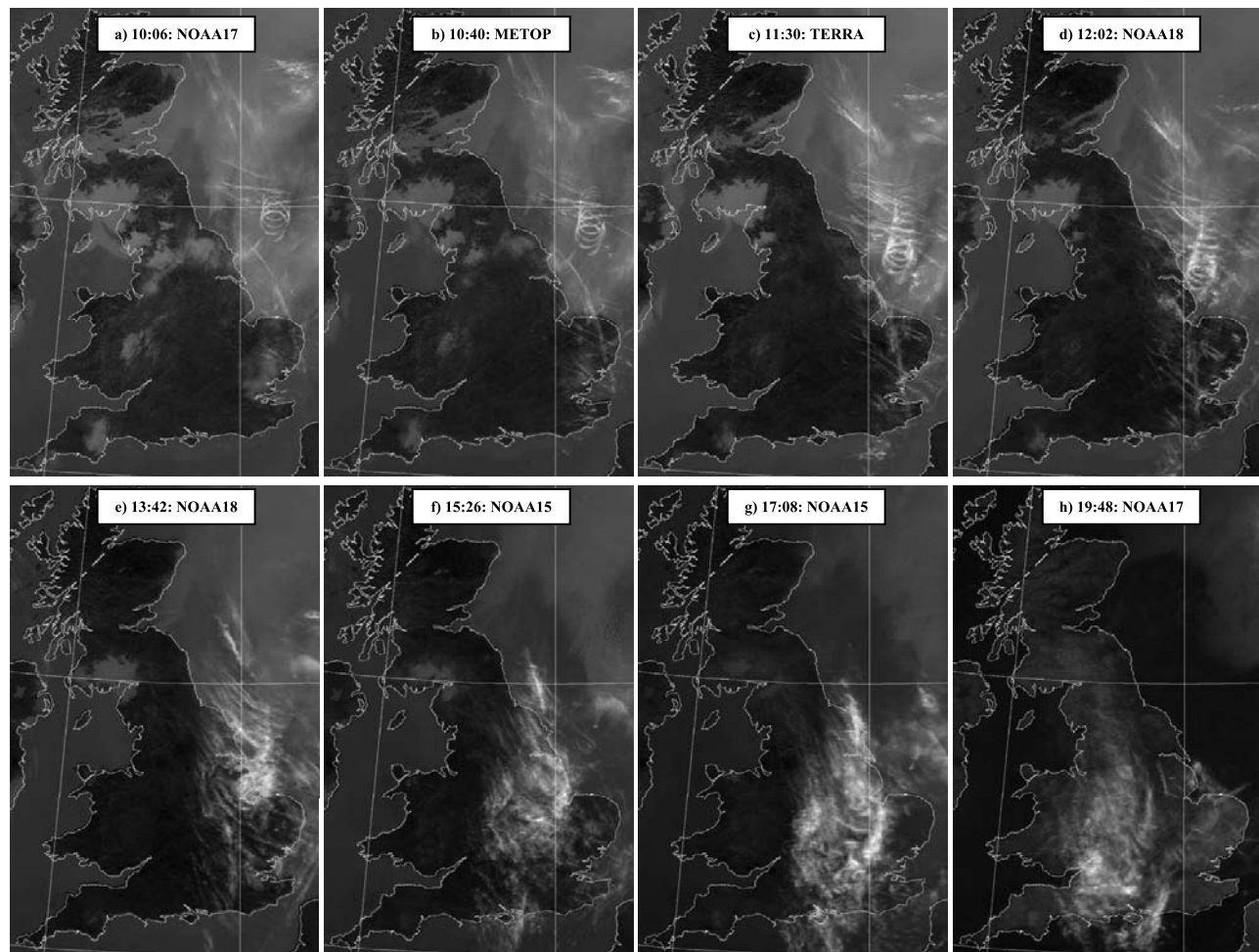
Figure 5. IR (10.8 μm) images of the formation of contrail induced cirrus (bright white). Areas of stratocumulus are shown as medium gray. The time and satellite is shown in the inset in each of the frames.

ECMWF forecast model fields of supersaturation shown in Figure 4b.

[12] The earliest image that shows the presence of the CCC is at 1006 UTC where five complete orbits are shown. By 1130 UTC the CCC has advected to the south but retains its characteristic shape which now contains 10 full orbits. Thus, one orbit takes approximately 17 min. By 1202 UTC, the CCC is becoming more difficult to identify owing to shear and diffusion smearing the characteristic shape of the CCC and by the mixing with other contrails. By 1526 UTC all initial resemblance to the coil shape has all but vanished and the casual observer would be forgiven for thinking that the resulting cirrus was an entirely natural feature; indeed, we are unable to definitively rule out the possibility that entirely natural cirrus could have formed anyway. The contrail-induced cirrus then persists over the United Kingdom until at least 1948 UTC and is advected southward over the Isle of Wight as shown by the final frame of Figure 5. Further imagery from 0332 UTC on 21 March 2009 (not shown for reasons of brevity) suggests that contrail-induced cirrus is still present over southwest England, although this cirrus was likely generated from contrails forming to the north and west of the distinctively shaped CCC.

[13] By considering the time evolution of the CCC, we can deduce that the first orbit would have been started at around 0830 UTC, and that the contrail formation from the aircraft ceased around 1150 UTC. To show beyond reasonable doubt that the CCC is still over the United Kingdom by 1948 UTC, we initiate the Met Office Numerical Atmospheric-dispersion Modeling Environment (NAME) model. NAME is a Lagrangian particle model [*Ryall and Maryon*, 1998] in which emissions from pollutant sources are represented by parcels released into a model atmosphere driven by the meteorological fields from the Met Office global, North Atlantic Environment, or UK4 NWP models. Each parcel carries mass of one or more pollutant species. The mass can change because of various physical and chemical processes during its life-span. Although originally designed as an emergency response nuclear accident model, subsequent development has greatly enhanced NAME's capabilities so that it is now used in a wide range of applications [*Jones*, 2004]. The NAME model was initiated using UK4 model data and emission rate of particulate mass of 1 g s^{-1} at an altitude of 30,000 ft (9 km) in a fixed circle centered on 55.3°N, 1°E with a radius of 20 km. The emission rate is entirely arbitrary and bares no resemblance to engine particulate or
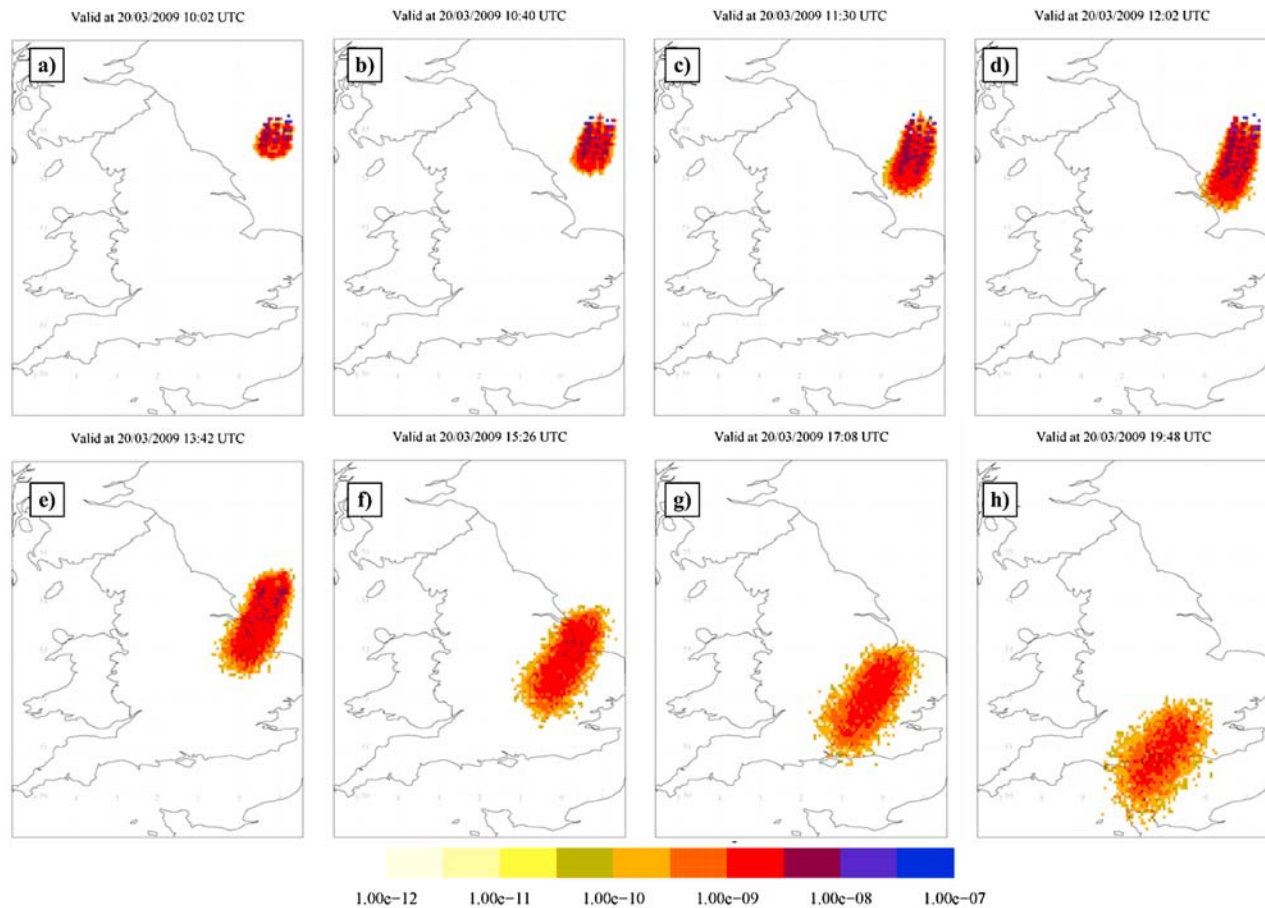
Figure 6. Results from the NAME model initiating a contrail circle at 30,000 ft during the period 0830 to 1150 UTC on 20 March 2009. The units are nominally g m^{-3} from an initial emission of 1 g s^{-1}.

water vapor emissions. In addition, the specific microphyscial evolution of contrail-induced cirrus is not modeled. While dynamical processes of turbulent diffusion and shear are included, the microphysical process of gravitational sedimentation of cirrus particles is not parameterized. As gravitational sedimentation is the major mechanism for the spreading of contrails in the vertical [e.g., *Burkhardt and Kärcher*, 2009], this deficiency is likely to result in the NAME simulations underestimating the geometric thickness of the resulting contrail-induced cirrus. The size and location of the circular orbit were determined by visual inspection of the satellite images. The results from the dispersion model are shown in Figure 6. Figures 6a–6c show that as in the satellite images shown in Figure 5, the modeled CCC is stretched in the N-S direction, and by 1202 UTC, the southernmost extent of the CCC is just over the coast of the United Kingdom near the Humber estuary. Between 1342 and 1526 UTC the CCC is directly over the Cardington field site (see Figure 1 for the location). By 1708 UTC the modeled CCC lies broadly between the Wash and the Isle of Wight and is roughly centered on the Isle of Wight by 1948 UTC.

[14] Throughout the first part of the period, the coherence of the CCC modeled by the NAME model and that observed by satellites is excellent which suggests that even

when the CCC becomes indistinct in the observations, the origin of the cirrus over the United Kingdom appears to be from persistent contrails. Tests with the NAME model, but with emissions now at 35,000 ft (10.5 km), reveal that the position of the modeled CCC is quite similar, with a similar spread and trajectory but ends in a slightly more easterly location (less than 50 km difference from that shown in Figure 6h) by 1948 UTC. Similarly, initiating the emissions at 25,000 ft (7.5 km) again leads to a more easterly position with the CCC being centered over London. Thus, although we cannot be certain, an emission height of 30,000 ft or 9 km appears to result in the best agreement between the model and satellite observations of the CCC.

[15] This choice of emission height can be validated by independent measurements made by the Doppler lidar at the Chilbolton Observatory (for location see Figure 1). Doppler lidar attenuated backscatter is shown in Figure 7. Any cirrus signature is entirely absent from the retrievals until around 1300 UTC, in agreement with what might be expected from the satellite observations of Figure 5. By 1500 UTC, what we believe to be tenuous persistent contrails/contrail-induced cirrus other than those formed from the CCC are evident. The CCC is forecast to influence the retrievals from around 1700 UTC (see Figures 6g and 6h), and continuous cirrus is
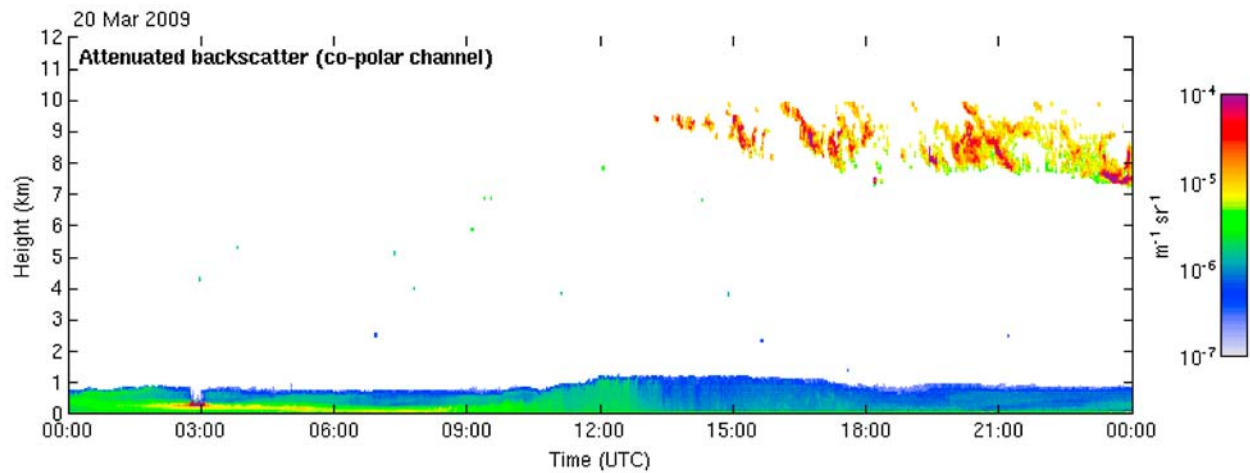
Figure 7. Showing the attenuated backscatter from the Chilbolton Doppler lidar for 20 March 2009. The main altitude of aviation-induced cirrus is seen to be between 8 and 9 km altitude.

indeed detected between 7.5 and 9.5 km between 1700 and 2400 UTC.

## 4. Determination of the Contrail-Induced Cirrus Optical Depth and Effective Radius

[16] *Minnis et al.* [1998] were able to assess the evolution of the contrail-induced cirrus particle radii, as small contrail particles grow to become indistinguishable from natural cirrus. Our efforts are hampered by the presence of low-level stratocumulus clouds below the contrails which make unique solutions to satellite inversion algorithms extremely challenging for operational retrievals, meaning that the particle size evolution cannot be evaluated when these low-level clouds are present. However, there are enough contrail/cirrus-influenced pixels over otherwise cloud-free oceanic areas to perform a limited set of retrievals. These retrievals make use of reflectance measurements at a pair of solar wavelengths (in this case the SEVIRI channels centered at 0.8 and 1.6 μm), following techniques developed by *Nakajima and King* [1990] and are produced routinely at the Met Office for every 15 min during daylight hours.

[17] Figure 8 shows images of the cloud optical thickness and effective radius retrieved from SEVIRI data for 1400 UTC. The large area of liquid water stratocumulus cloud over the northern part of the North Sea is apparent, and it is this optically thick low cloud that the retrieval scheme has identified, rather than the overlying optically thin ice cloud. The areas free of low-level water cloud off the east coast of England are identified as ice cloud made up of aggregate particles having optical thicknesses generally less than around 2. Because of the thin nature of the ice cloud, the retrieval scheme encounters problems over land and incorrectly identifies much of the thin cloud over eastern England as being water cloud. For this reason, all land pixels identified as being water cloud with an optical thickness less than 4 have been classed as ice cloud in Figure 8a when used in subsequent calculations and the corresponding effective radius pixels have been flagged as invalid data in Figure 8b.

[18] Frequency histograms of the optical thickness and effective radius are shown in Figure 9, the data here being restricted to only ice cloud retrievals over sea. Two areas are considered, the small area 52.25°N to 54.6°N, 0.7°W to 1.4°E associated with the CCC in Figures 5 and 6 (and shown as a cyan box in Figure 8a), and the larger (L) area 50°N to 58°N, 3°W to 5°E to tie in with the main area of ice cloud shown in Figure 8a, where this area is shown as a magenta box. Figure 9a shows a distribution of optical thicknesses in the CCC (dotted curve) ranging between 0.4 and 1.95, with a mean value of 1.06, whereas the distribution of optical thicknesses for the residual (i.e., L minus CCC) area (solid curve) shows significantly lower values, the mean value being 0.74. Corresponding effective radius distributions are shown in Figure 9b, and these indicate that the values in the CCC area (dotted curve) are generally lower than those in the residual area (solid curve), with a mean value of 27.9 μm for the CCC area and a mean value of 35.2 μm for the residual area. The ice water path retrievals (not shown) suggest a mean value of 17.8 g m^{-2} for the CCC area and a mean value of 15.7 g m^{-2} for the residual area. If we assume that the contrail-induced cirrus is of 1–2 km thickness (as in the lidar profile shown in Figure 7), then an ice water content of 8–18 mg m^{-3} is derived which corresponds to values between the median and the upper quartile measured in midlatitudes of the Northern Hemisphere at temperatures between −43°C and −53°C during the Interhemispheric Differences in Cirrus Properties From Anthropogenic Emissions (INCA) measurement campaign [*Gayet et al.*, 2004].

[19] A scatterplot of the optical thickness versus the ice effective radius is shown in Figure 9c for the CCC (red dots) and the residual area (black dots). Smaller ice effective radii are associated with optically thicker cirrus of the CCC. *Minnis et al.* [1998] report a change in contrail-induced cirrus cloud effective radius from around 10 μm at contrail formation to around 30 μm after approximately 7.5 h. In our analysis, the oldest cirrus particles are around 5–6 h old; our values of around 28 μm are in reasonable agreement, although the rate of increase of particle size will be strongly dependent on the atmospheric conditions [*Fahey et al.*,
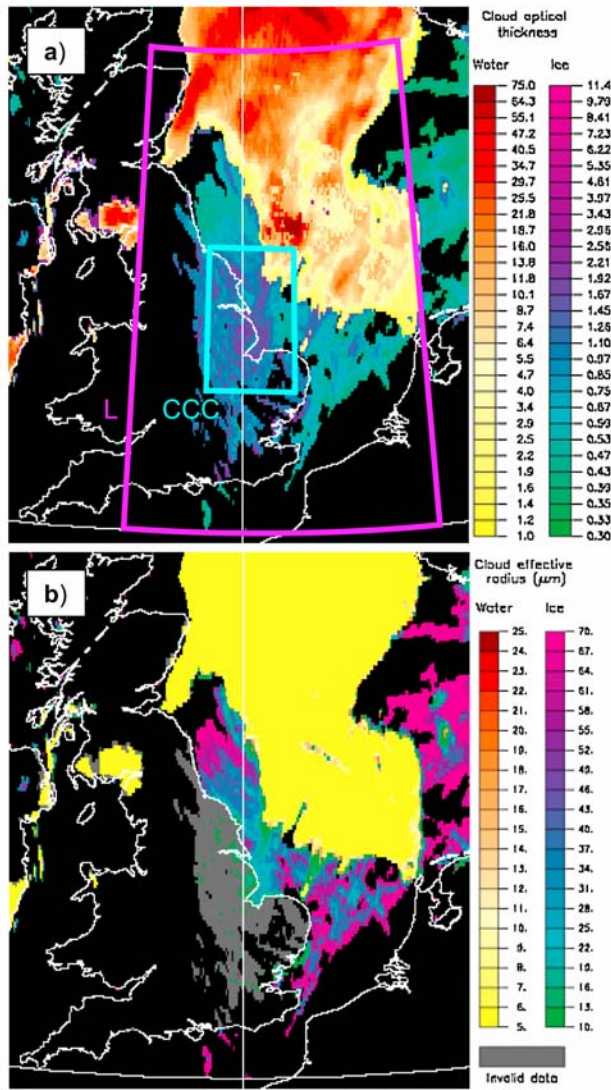
Figure 8. Retrievals of the (a) visible (∼0.55 μm) cloud optical thickness and (b) effective radius (μm) for 1400 UTC on 20 March 2009. The left and right scales on each plot are for water cloud and for ice cloud, respectively. The coil-shaped contrail/cirrus (CCC) and larger (L) areas referred to in the text are shown in Figure 8a as cyan and magenta boxes, respectively.

1999]. The cause of the difference in the microphysical properties of the CCC is not investigated here but could be due to the higher concentration of ice nuclei emitted owing to circling nature of the aircraft flight pattern or the lower estimated air speed of the AWACS operations (estimated from the time taken to complete one complete circle of radius 20 km as around 440 km h^{-1}) compared to aircraft operating at faster cruising speeds.

5. Determination of the Solar SW Radiative Forcing From the Contrail-Induced Cirrus at the Surface

[20] The radiative forcing of the contrail-induced cirrus is determined from the Cardington field site (location shown
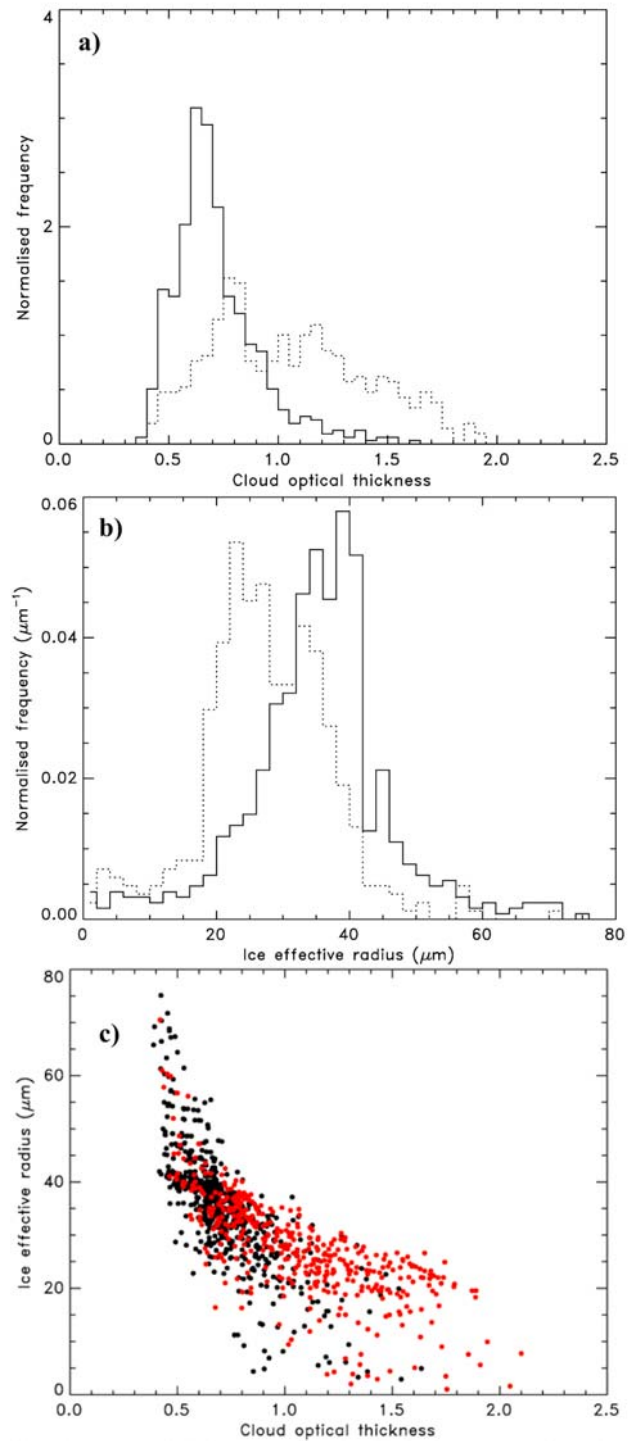
Figure 9. Frequency distributions of (a) the cloud optical depth and (b) cloud top ice effective radius at 1400 UTC. For each plot, the solid curve shows the ice cloud properties derived over the residual area (i.e., L minus CCC), while the dotted curve shows properties derived for the CCC area. (c) A scatterplot of the ice effective radius against the cloud optical thickness. Black dots indicate points from the residual area, and red dots indicate points from the CCC area.

in Figure 1) using standard Eppley solar pyranometers. Detection of the radiative effects of the contrail-induced cirrus at infrared wavelengths is not considered here because the variation in water vapor dominates the infrared signal. Figure 5 shows that Cardington will be affected both by the CCC and by contrail-induced cirrus from other sources. However, the NAME modeling of the CCC suggests that Cardington will become directly influenced by the CCC sometime between 1410 and 1430 UTC. We estimate the radiative forcing in two separate ways.

[21] 1. Determining the downwelling solar irradiance including contrail-induced cirrus from 20 March 2009 ($SW_{\downarrow 20 \text{ obs}}$) and using simple radiative transfer modeling to determine the surface irradiance in the absence of contrail-induced cirrus ($SW_{\downarrow 20 \text{ model}}$). The surface SW radiative forcing by contrail-induced cirrus, ΔF_{SW}, is then given by

$$\Delta F_{SW \text{ obs and model}} = SW_{\downarrow 20 \text{ obs}} - SW_{\downarrow 20 \text{ model}}. \quad (1)$$

Because the radiative transfer modeling only needs to account for Rayleigh scattering and gaseous absorption, only a very simple radiative transfer parameterization scheme is used. Rayleigh scattering and gaseous absorption by ozone and water vapor are accounted for using the parameterizations for atmospheric transmission developed by *Lacis and Hansen* [1974] including a magnification factor to account for the curvature of the Earth and refraction of incident radiation [*Rodgers*, 1967]. Ozone is estimated from the Ozone Mapping Imager (OMI) to be around 325 Dobson unit (1 DU = 0.001 atm cm), while the precipitable water vapor is from the nearby Nottingham radiosonde.

[22] 2. Determining the downwelling SW irradiance including contrail-induced cirrus from 20 March 2009 ($SW_{\downarrow 20 \text{ obs}}$) and using observations from a cloud and contrail-free day (18 March 2009) to determine the surface irradiance from observations in the absence of contrail-induced cirrus ($SW_{\downarrow 18 \text{ obs}}$). The surface SW radiative forcing by contrail-induce cirrus, ΔF_{SW}, is then given by

$$\Delta F_{SW \text{ obs}} = SW_{\downarrow 20 \text{ obs}} - SW_{\downarrow 18 \text{ obs}}. \quad (2)$$

The precipitable water vapor varies from 8.3 cm on 18 March 2009 at 1200 UTC to 5.2 cm on 20 March at 1200 UTC for the Nottingham ascent. This change in water vapor can contribute significantly to differences in the SW radiation reaching the surface: calculations using the parameterizations of *Lacis and Hansen* [1974] indicate a maximum difference at local noon of around 16 W m^{-2}. This change in downwelling SW irradiance because of changes in column water vapor loading is accounted for in our calculations.

[23] Figure 10a shows the ratio of the diffuse to the direct fluxes between 1400 and 1800 UTC for 18 March 2009 (contrail and cloud free) and 20 March 2009 (affected by contrail-induced cirrus but otherwise cloud free). The effect of contrail-induced cirrus can clearly be seen on 20 March 2009 with a significant increase in the diffuse to total radiation at the surface. The more variable nature of the diffuse to total radiation caused by the varying contrail-

induced cirrus optical depth and viewing geometries can also be seen in the data from 20 March when compared to 18 March.

[24] Figure 10b shows $\Delta F_{SW \text{ obs}}$ and $\Delta F_{SW \text{ obs and model}}$ determined from the two methods described above which show reasonable agreement. The peak ΔF_{SW} is determined to be stronger than -150 W m^{-2} (the minus sign indicating a reduction in SW radiation at the surface). Subsequently, ΔF_{SW} is weaker, ranging from around 0 to -50 W m^{-2}. Between 1400 and 1700 UTC the mean $\Delta F_{SW \text{ obs}}$ is -44 W m^{-2} and the mean $\Delta F_{SW \text{ obs and model}}$ is -47 W m^{-2}. Although the modeling method tends to give a slightly higher mean estimate for ΔF_{SW}, no consistent bias is found (e.g., the period between 1500 and 1600 UTC), and either method may be thought of as a reasonable approximation. A standard deviation of 14 W m^{-2} is found for both methods, when considering 1 min averages, leading to a standard error of around 1 W m^{-2}. The real error is considerably higher owing to potential systematic uncertainties in the total column water vapor and ozone fields and variations in the aerosol optical depth and is estimated as ±10 W m^{-2}.

6. Determination of the SW and LW Radiative Forcing of Contrail-Induced Cirrus at the Top of the Atmosphere

[25] The radiative forcing is determined at the top of the atmosphere by using a methodology similar to that used by *Haywood et al.* [2005]. *Haywood et al.* [2005] compared the LW top of the atmosphere clear-sky irradiances derived from the Meteosat-7 instrument with those predicted by the Met Office global NWP model. Differences in the irradiances of up to 50 W m^{-2} were clearly identified over the Sahara. This feature was shown to be due the omission of the radiative effects of mineral dust in the NWP model. Here we perform a similar exercise; because the NWP model does not accurately represent the ice supersaturation observed between approximately 25,000–35,000 ft (7.5 to 10.5 km) (Figure 3b), no cirrus cloud is modeled in these regions. Just as the study of *Haywood et al.* [2005] does not rely on explicit modeling of the radiative effects of mineral dust, the simulations that we perform here do not rely on explicit modeling of the radiative effects of contrail-induced cirrus. The estimates presented here are therefore independent of the retrievals derived in section 4.

6.1. Definition and Diagnosis of the Radiative Forcing

[26] The radiative forcing at the top of the atmosphere (TOA), ΔF_{SW_TOA}, of the contrail-induced cirrus can be simply diagnosed as
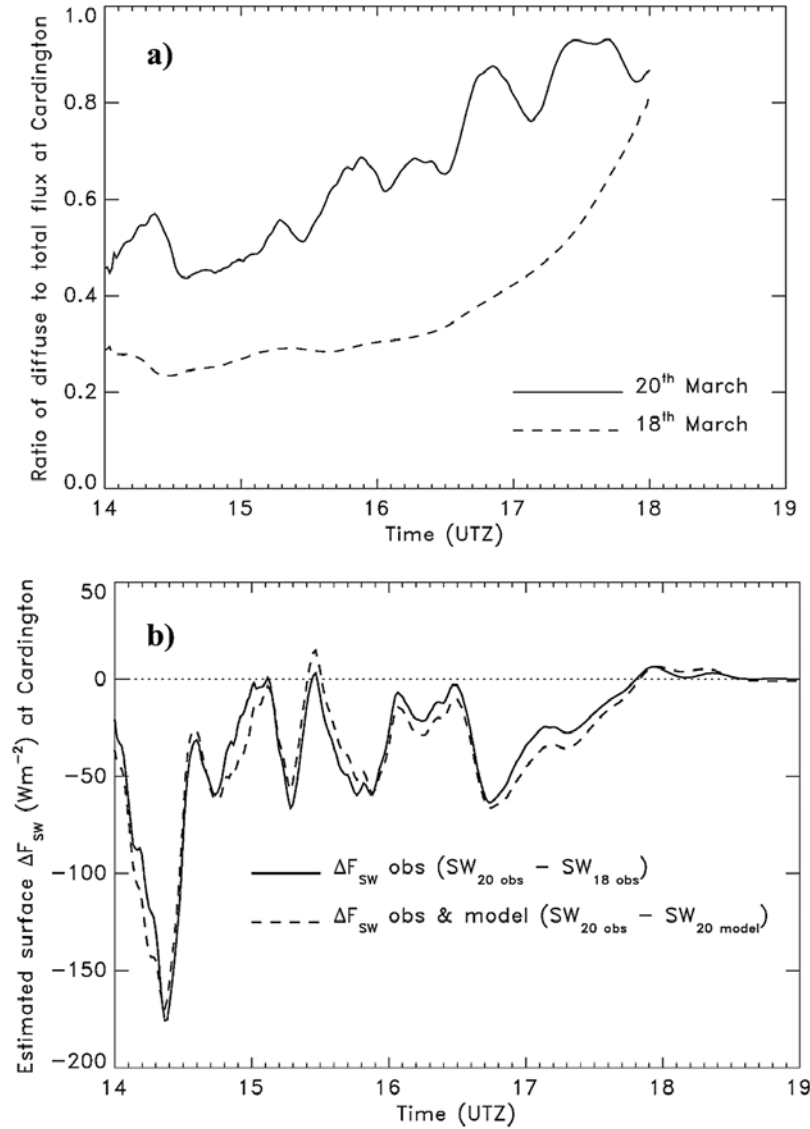
$$\Delta F_{SW\_TOA} = SW_{\uparrow \text{no contrails}} - SW_{\uparrow \text{contrails}} \quad (3)$$

or

$$\Delta F_{SW\_TOA} = SW_{\uparrow \text{model}} - SW_{\uparrow \text{satellite}}. \quad (4)$$

Similarly the longwave radiative forcing, ΔF_{LW_TOA}, can be diagnosed from

$$\Delta F_{LW\_TOA} = LW_{\uparrow \text{no contrails}} - LW_{\uparrow \text{contrails}} \quad (5)$$

Figure 10. Showing (a) the ratio of diffuse to total downward solar irradiance for 20 March 2009 (contrail case) and for 18 March 2009 (no contrails), and (b) the estimated change in the downward surface irradiance (W m^{-2}) at Cardington derived using two different methods (see text for details).

or

$$\Delta F_{LW\_TOA} = LW_{\uparrow model} - LW_{\uparrow satellite}. \qquad (6)$$

Previous studies have derived top of the atmosphere irradiances from radiance data from either the Meteosat-7 instruments [*Haywood et al.*, 2005] or the Geostationary Earth Radiation Budget (GERB) instrument [*Allan et al.*, 2007]. In this study we diagnose SW$_{\uparrow satellite}$ and LW$_{\uparrow satellite}$ from the SEVIRI instrument. Broadband irradiance is routinely estimated from narrowband channels of the SEVIRI instrument by the Royal Meteorological Institute of Belgium in the processing of GERB data. Processing is conducted on 3 × 3 SEVIRI pixels at an approximate pixel resolution over the United Kingdom of 15 km. Conversion of narrow to broadband radiances is achieved using a regression technique combined with detailed calculations

from line-by-line radiative transfer simulations [*Clerbaux et al.*, 2008a] and are converted to irradiance using a set of angular distribution models; this is essentially the same method as described by *Haywood et al.* [2005] for Meteosat-7 but exploiting the greater number of channels supplied by SEVIRI. For the shortwave region of the spectrum, a similar approach is adopted, using three shortwave channels from SEVIRI in the regression and applying angular dependence models from the Clouds and the Earth's Radiance Energy System (CERES) data set to estimate broadband shortwave irradiance [*Clerbaux et al.*, 2008b].

[27] Since GERB data were only produced between 0200 and 0700 UTC during the period of interest, we use the SEVIRI-based estimates of SW$_{\uparrow satellite}$ and LW$_{\uparrow satellite}$. To reduce the effect of slight timing differences between the model and the SEVIRI data, SW$_{\uparrow satellite}$ is scaled by the ratio

of the incoming shortwave radiation for the model and the satellite data.

[28] Interpolating SEVIRI LW$_{\uparrow \text{satellite}}$ to the GERB grid, comparisons were conducted over 140 grid points over the UK region for 0300 and 0600 UTC on the 20 and 21 March 2009. A mean bias of 0.7 W m^{-2} and root-mean-square difference of 3.2 W m^{-2} between SEVIRI and GERB estimates are apparent. On the basis of the expected SEVIRI calibration and the processing described by *Clerbaux et al.* [2008a, 2008b], we propose a conservative estimate of uncertainty of order 5%, which corresponds to ±12.5 W m^{-2} for an irradiance of 250 W m^{-2}; a similar uncertainty is assumed for SW$_{\uparrow \text{satellite}}$.

[29] To diagnose SW$_{\uparrow \text{model}}$ and LW$_{\uparrow \text{model}}$, we use the TOA fluxes from the high-resolution operational UK4 model [*Lean et al.*, 2008] which has a spatial resolution of 4 km in the horizontal and contains 70 model levels. The model is initialized at 0000 UTC and is run forward with no data assimilation for a period of 36 h. Data assimilation is turned off to prevent the model from moistening the upper troposphere via assimilation of observational data sets, and hence, we deliberately inhibit any cirrus cloud formation. The model time step is 100 s with radiation being called every 9 time steps (15 min). The model contains a basic aerosol climatology [*Cusack et al.*, 1998]. The SW surface reflectance is determined from the combined reflectance of nine representative surface types as described in the Met Office Surface Exchange Scheme II (MOSES II) [*Essery et al.*, 2003], and the surface emissivity is uniformly set to a spectrally independent value of 0.97. The radiation scheme in the model is the *Edwards and Slingo* [1996] radiation code which is configured to treat the absorption and scattering of SW and LW radiation by gases, aerosols, and water and ice clouds. The radiation code contains five bands in each of the SW and LW regions of the spectrum, and the two-stream approximation is used. Note here that the irradiances derived from the UK4 model are very similar to those from the global model; we chose to present the analysis of the UK4 model only as this model has superior spatial resolution.

[30] Sources of error in SW$_{\uparrow \text{model}}$ and LW$_{\uparrow \text{model}}$ come from errors in both the parameterization of radiation (e.g., the two-stream approximation and the relatively coarse spectral resolution used in the operational model [*Edwards and Slingo*, 1996]) and from errors in the horizontal and vertical spatial distribution of gases that absorb radiation in the SW and LW region of the spectrum. One specific potential error relating to the latter is the low bias in the upper tropospheric water vapor in the model fields which may bias SW$_{\uparrow \text{model}}$ and LW$_{\uparrow \text{model}}$. Calculations with a stand-alone version of the *Edwards and Slingo* [1996] radiation code where the upper troposphere between 200 and 500 hPa is moistened from the subsaturated profile from the Nottingham ascent (Figure 3b) to that of the supersaturated Ekofisk ascent reveal a negligible effect on SW$_{\uparrow \text{model}}$, but a bias of up to +5 W m^{-2} for LW$_{\uparrow \text{model}}$. However, we shall see that a bias of this magnitude is a second-order effect when we isolate the $\Delta F_{\text{TOA\_LW}}$ of contrails.

6.2. Approach to Cloud Screening

[31] The cloud screening approach that is used here differs when applied to satellite and the model data. Low-lying stratocumulus clouds have less impact on LW radiation than SW radiation at the top of the atmosphere because the temperature of the top of the low-level liquid water clouds is only a few degrees different from the surface of the ocean whereas the change in the SW reflectivity change can be significant. Consider the tephigrams in Figure 3, particularly the Ekofisk ascent in the North Sea. Although no stratocumulus cloud was present at this location, the relative humidity was 88% at 993 hPa. The difference between the temperature at 993 and 1026 hPa (the highest recorded pressure approximately corresponding to 29 m altitude) was less than 4 K. Calculations show that differences of 4–6 K at temperatures of around 280 K correspond to flux differences of around 6–9% or 13–20 W m^{-2} for TOA fluxes of 220 W m^{-2}. Thus, in terms of TOA LW irradiances, areas where stratocumulus cloud is forecast in the model but not present in the observations (or vice versa) will lead to an error estimated as approximately ±20 W m^{-2}. We therefore assign an error estimate of ±20 W m^{-2} over areas where cloud is present in either the model or the satellite retrievals.

[32] For SW$_{\uparrow \text{satellite}}$ over oceans, areas where the cloud retrievals described in section 4 reveal the influence of low-level water cloud are screened out of the analyses. Over land, for optically thin clouds, the retrievals fail (section 4), and liquid water cloud is diagnosed. This problem is overcome by applying a threshold that removes all areas of liquid cloud with optical thickness at 0.55 μm greater than 2. For SW$_{\uparrow \text{model}}$, areas with significant liquid water cloud are screened out from the data. While it is recognized that these masking thresholds have some degree of subjectivity associated with them, the results presented in section 6.3 appear entirely reasonable.

6.3. Results

[33] The resulting LW$_{\uparrow \text{satellite}}$, LW$_{\uparrow \text{model}}$, and $\Delta F_{\text{LW\_TOA}}$ with no cloud screening applied are shown for 1400 UTC in Figures 11a, 11b, and 11c, respectively. Figure 11a shows LW$_{\uparrow \text{satellite}}$ of greater than 260 W m^{-2} over land areas of the United Kingdom and the continent. Lower values of around 250 W m^{-2} are evident in clear skies over the ocean owing to the lower surface temperature. The lowest values of all are apparent over the North Sea and over eastern areas of England where a LW$_{\uparrow \text{satellite}}$ of less than 220 W m^{-2} is evident; these areas correspond to the presence of either thick low-level stratocumulus clouds, or thin high-level contrail-induced cirrus. Figure 11b indicates that LW$_{\uparrow \text{model}}$ shows many similar features to LW$_{\uparrow \text{satellite}}$; the highest values over land regions, lower values over clear-sky ocean regions, and the lowest values over thick modeled stratocumulus regions are all present. The feature that is clearly absent is the low values (<220–230 W m^{-2}) associated with the optically thin contrail-induced cirrus. $\Delta F_{\text{LW\_TOA}}$ obtained from equation (6) shows strong positive values which exceed +40 W m^{-2} in the vicinity of the CCC (see area "i" on Figure 11c). The strong spatial correlation between $\Delta F_{\text{LW\_TOA}}$ and the polar orbiting satellite image of the CCC shown in Figure 5e and the modeled position of the CCC shown in Figure 6e is clearly evident. A second area where $\Delta F_{\text{LW\_TOA}}$ exceeds +40 W m^{-2} is also shown in Figure 11c (area "ii") which appears to correspond to contrails initiated off the east coast of Scotland (see
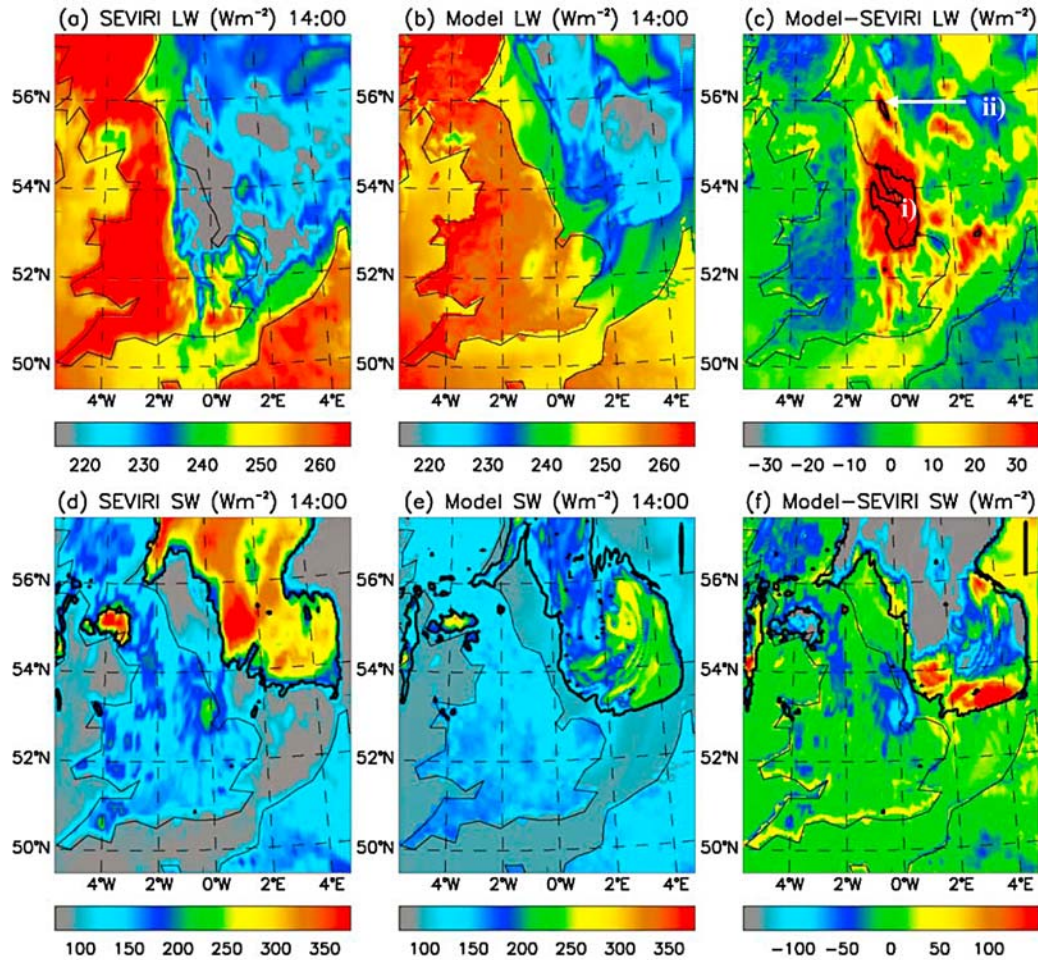
Figure 11. Showing (a) $LW_{\uparrow \text{satellite}}$, (b) $LW_{\uparrow \text{model}}$, (c) ΔF_{LW_TOA}, (d) $SW_{\uparrow \text{satellite}}$, (e) $SW_{\uparrow \text{model}}$, and (f) ΔF_{SW_TOA} for the top of the atmosphere for 1400 UT for 20 March 2009. In Figure 11c the contour interval represents $\Delta F_{LW\_TOA} > 40$ W m^{-2}. In Figures 11d, 11e, and 11f, the contour encompasses areas of liquid water cloud (see text for details of the cloud screening procedure).

Figure 5). There are several areas where ΔF_{LW_TOA} is diagnosed as being negative; areas of SW England, Wales, northern Scotland and the continent all exhibit ΔF_{LW_TOA} as strong as -15 W m^{-2}. Interestingly, no significant biases are evident over clear-sky ocean areas. The biases over land areas are likely related to a cold bias in the surface temperature in the UK4 model (J. M. Edwards, personal communication, 2009) which is currently under investigation but beyond the scope of the present work.

[34] The resulting $SW_{\uparrow \text{satellite}}$, $SW_{\uparrow \text{model}}$, and ΔF_{SW_TOA} with no cloud screening applied are shown for 1400 UTC in Figures 11d, 11e, and 11f, respectively. It is immediately apparent that the differences between the modeled and measured irradiances over the stratocumulus clouds in the North Sea are far larger in the SW region of the spectrum than in the LW region, with SEVIRI generally diagnosing brighter clouds by in excess of 150 W m^{-2} in many areas. The liquid water cloud mask for SEVIRI (sections 4 and 6.2) are encompassed by the thick contour intervals on Figure 11d surrounding the extensive stratocumulus in the North Sea and another less extensive area of stratocumulus over southwest Scotland. Liquid water cloud present in the model is encompassed by the thick contour line shown in

Figure 11e. Generally, the model does a reasonable job of predicting the presence and areal extent of the stratocumulus regions in both the North Sea and SW Scotland. There are areas where the model contains cloud where the SEVIRI retrieval does not or vice versa. For example the model extends the stratocumulus sheet in the North Sea further south than the SEVIRI retrieval and SEVIRI shows more extensive stratocumulus to the extreme northwest of the images shown. The composite cloud mask determined in Figure 11f contains all areas where liquid water cloud is diagnosed in either the SEVIRI retrieval or the model and is indicated once more by areas falling within the thick contour line. This composite cloud screening algorithm is used henceforth in screening data for liquid water cloud via a simple cloud mask.

[35] ΔF_{LW_TOA} and ΔF_{SW_TOA} including the cloud mask are shown in Figure 12 for the period 1200 to 1800 UTC. No ΔF_{SW_TOA} is shown for 1800 UTC because the Sun had set. The areas of maximum ΔF_{LW_TOA} and ΔF_{SW_TOA} associated with the contrail-induced cirrus are shown to drift southward in agreement with the observations in Figure 5 and the modeling in Figure 6. ΔF_{LW_TOA} has values stronger than 45 W m^{-2} throughout the period
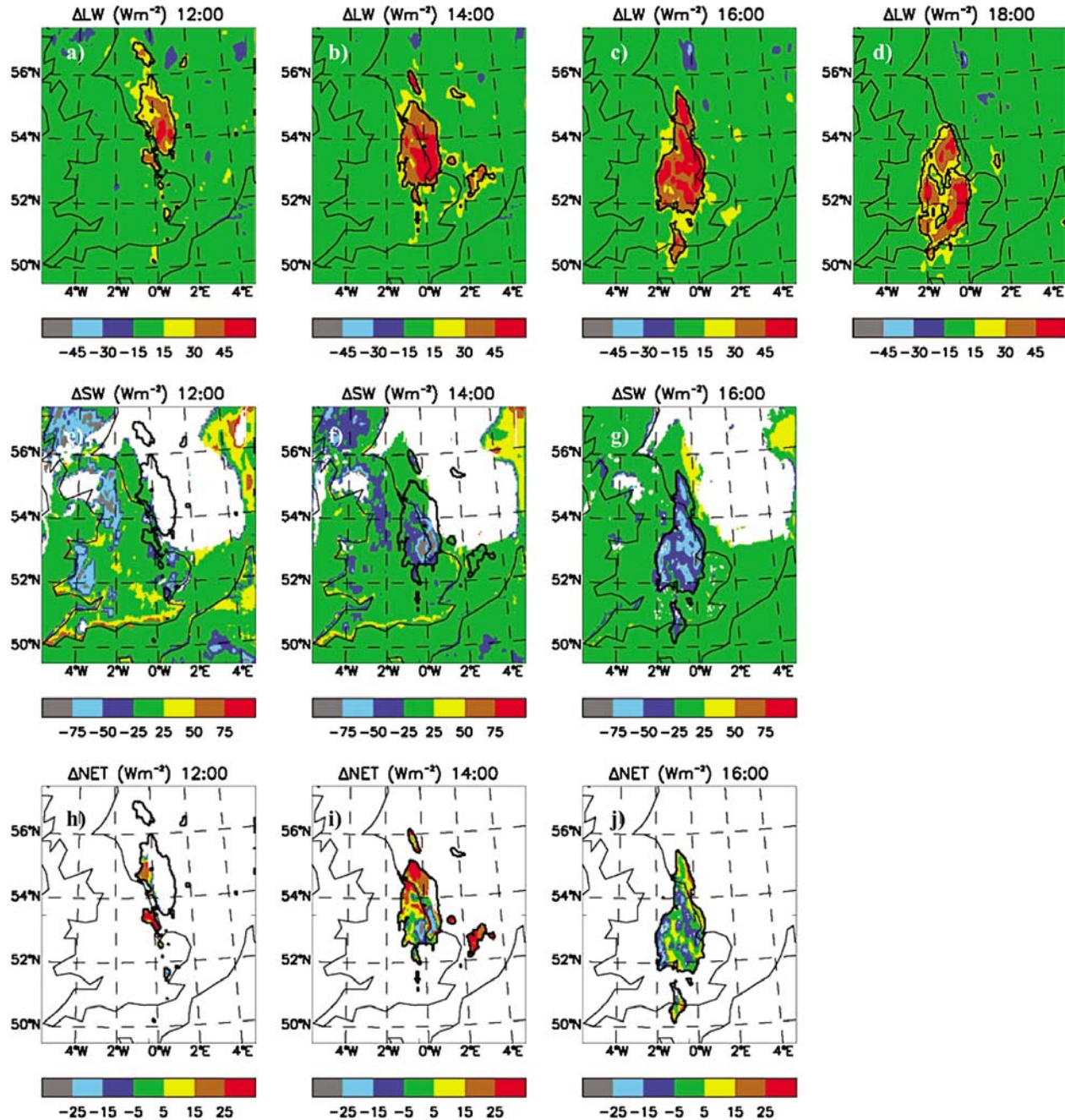
**Figure 12.** Showing (a–d) the evolution of ΔF_{LW_TOA}, (e–g) ΔF_{SW_TOA}, and (h–j) ΔF_{net_TOA} on the 20 March 2010. The contour line marked on the figures shows areas defined as contrail as described in the text.

(Figures 12a–12d). On the other hand, ΔF_{SW_TOA} shows values stronger than -75 W m^{-2} in the predicted position of the CCC at 1400 UTC (Figure 12f). As a consequence, there is significant cancellation of ΔF_{LW_TOA} and ΔF_{SW_TOA} as is clearly shown in ΔF_{net_TOA} (Figures 12h–12j). The temporal evolution of the mean ΔF_{LW_TOA}, ΔF_{SW_TOA}, and ΔF_{net_TOA} over the domain encompassed by the thick contour on Figure 12 are shown in Figure 13a.

[36] Figure 13a shows that during daylight hours ΔF_{LW_TOA} is significantly offset by ΔF_{SW_TOA} leading to a ΔF_{net_TOA} of around $+10$ W m^{-2} during the period 1100–1500 UTC. ΔF_{net_TOA} becomes negative when the solar

zenith angle increases toward sunset owing to the stronger contribution from the SW component as expected from detailed radiative modeling of the SW and LW radiative effects [*Myhre and Stordal*, 2001]. At sunset ΔF_{net_TOA} is simply equal to ΔF_{LW_TOA}. Note that ΔF_{SW_TOA} becomes more negative during afternoon until immediately before sunset, at a rate that is faster than the ΔF_{LW_TOA} becomes more positive. This is consistent with the increase in SW forcing, due to the dependence of the contrail albedo on solar zenith angle, as was discussed by, for example, *Myhre and Stordal* [2001].
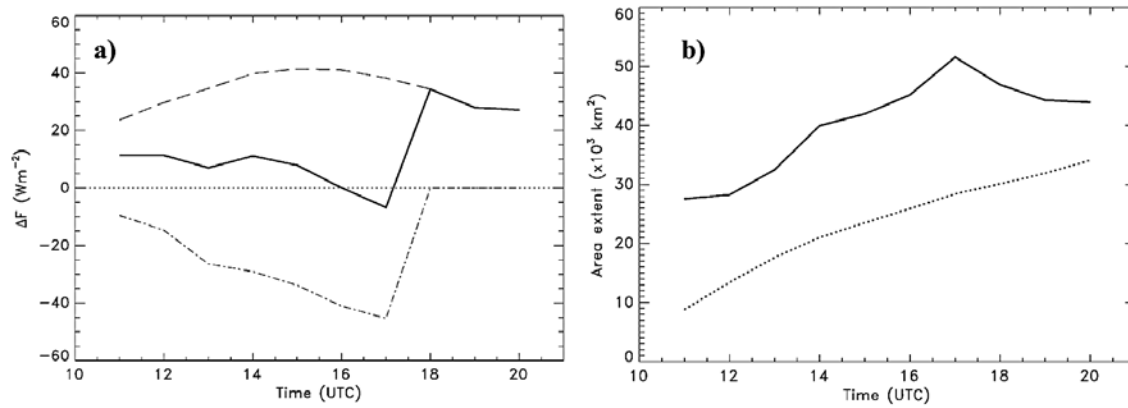
Figure 13. (a) ΔF_{LW_TOA}, ΔF_{SW_TOA}, and ΔF_{net_TOA} determined in the area marked by the solid contour on Figure 12 as described in the text. (b) The areal extent of the contrail-induced cirrus (in 1000s of km^2) determined from ΔF_{LW_TOA} (solid curve) and for the CCC determined from the NAME model (dotted curve) as a function of time.

[37] The areal extent of the contrail-induced cirrus is defined as areas where ΔF_{LW_TOA} is greater than twice the standard deviation of ΔF_{LW_TOA} in the domain shown in Figure 12 for each time frame. Alternative thresholds based on the standard deviation or even a single threshold could be applied, but our method has the advantage of factoring in the temporal variability of ΔF_{LW_TOA}. Figure 13b shows that the area extent of the contrail-induced cirrus steadily increases from around 28,000 km^2 at 1100 UTC to 52,000 km^2 by 1700 UTC after which it decays. Note that no areas outside the domain shown are classified as contrail-induced cirrus throughout the sequence shown, indicating that the cirrus has not simply advected out of the domain. Thus, the area of the contrail-induced cirrus approximately doubles in size over a 6 h period. We also calculate the area extent of the CCC from the NAME model results: these are also shown on Figure 13b. The CCC covers approximately 9000 km^2 at 1100 UTC, growing to approximately 34,000 km^2 by 2000 UTC and is on average 23,000 km^2. The rate of increase in the area is similar between the contrail-induced cirrus derived over the entire domain and that derived for the CCC until around 1700 UTC. After 1700 UTC the areal extent of the CCC derived from NAME continues to grow while the area of contrail-induced cirrus over the domain starts to diminish. This indicates that conditions for continued contrail-induced cirrus growth cease around this time. The reasons for this transition from conditions of contrail-induced cirrus growth to conditions of contrail-induced cirrus decay are unclear but could be due to a combination of a reduction in the magnitude and/or extent of the supersaturated area, sedimentation of ice crystals [e.g., *Burkhardt and Kärcher*, 2009] and the expected diurnal reduction in the air traffic activity in the area which could reduce new contrail formation [e.g., *Stuber et al.*, 2006].

[38] ΔF_{LW_TOA}, and ΔF_{SW_TOA} may also be calculated for the Cardington site. Because the scattering of visible radiation by contrail-induced cirrus should be essentially conservative, ΔF_{SW_TOA} should be roughly comparable to ΔF_{SW} determined at the surface (see section 5 and Figure 10). This comparison will be affected by the amount of absorption of near-IR by water vapor in the column between the CCC and the surface. ΔF_{SW_TOA} is evaluated from the 7 grid

boxes closest to Cardington, for 1200 UTC and at each hour through to sunset at around 1800 UTC; the mean value for ΔF_{SW_TOA} over the period 1400–1700 UTC is −36.5 W m^{-2}, which is in reasonable agreement with the surface ΔF_{SW} of between −44.4 to −47.3 W m^{-2} ± 10 W m^{-2} determined from the in situ measurements. As in the calculations over the entire domain (Figure 12), ΔF_{LW_TOA} for the same period for the Cardington site reveals an almost complete cancellation of the SW and LW effects with ΔF_{LW_TOA} being computed as +35.3 W m^{-2}.

7. Discussion and Conclusions

[39] The formation of persistent contrails and their evolution into contrail-induced cirrus clouds are illustrated. While it is not possible to be 100% certain that cirrus clouds would not have formed in the absence of aviation activity, the balance of evidence, which includes the spatial coherence of the contrail-induced cirrus and modeling its position, very strongly suggests that the cirrus cloud is of aviation origin.

[40] The persistence of the contrails and contrail-induced cirrus is remarkable. The persistent contrail formed at ∼0830 UTC on 20 March 2009 (Figures 5 and 6) is still clearly evident as contrail-induced cirrus some 12 h after formation. In fact, as noted in section 4, contrail-induced cirrus initiated during daylight hours of 20 March are clearly present in satellite imagery at 0332 UTC on 21 March 2009. The recent global modeling study of *Burkhardt and Kärcher* [2009] suggests that contrail-induced cirrus coverage is dominated by a few major events and that contrail-induced cirrus coverage scales with ice supersaturation rather than contrail coverage. Our study documents one such major event, which at its peak covers more than 50,000 km^2.

[41] Our study confirms the fact ΔF_{net_TOA} from contrail-induced cirrus is the relatively small residual derived from strong ΔF_{LW_TOA} and ΔF_{SW_TOA} components of opposite signs which has been known for some time [e.g., *Fahey et al.*, 1999, and references therein; *Stuber et al.*, 2006]. However, to our knowledge, this is the first time that this has been proved without relying on explicit modeling of contrail-induced cirrus microphysics. While our results have

to be considered to be a specific case study, it does question the merits of rescheduling aircraft flights from night to day flights which have been suggested to make maximum benefit of the negative radiative forcing owing to the reflection of solar radiation [e.g., *Myhre and Stordal*, 2001; *Stuber et al.*, 2006]. If contrails spread into contrail-induced cirrus and the cirrus has a lifetime of some 18 h as in this study, then initiating the contrail between 0000 and 0600 UTC on the 20 March 2009 would maximize the exposure of the contrail-induced cirrus to solar radiation. While, this calculation must be considered very speculative given our current understanding of the complexities of contrail-induced cirrus, the recent idealized global modeling study of *Burkhardt and Kärcher* [2009] supports the significant lag of contrail-induced cirrus behind aircraft operations. *Burkhardt and Kärcher* [2009] model emissions from transatlantic air traffic and find that contrail-induced cirrus peaks some 9 h subsequent to cessation of flying. Figure 5 suggests that the majority of fresh contrails in the study presented here were initiated between 0830 and 1200 UTC and the peak contrail-induced cirrus areal coverage (Figure 13b) is around 1700 UTC or some $5-9$ h subsequent to initiation.

[42] It is interesting to ask to what degree the radiative forcing from aviation is enhanced owing to the formation of the contrail-induced cirrus in this episode; here we make a simple estimate by considering solely the influence of the CCC that we presume is formed by the AWACS aircraft. We chose to compare our estimate of the radiative forcing against that from persistent contrails from the entire aviation fleet, as to compare against the radiative forcing from other emissions such as carbon dioxide would be misleading because of the disparate residence times of contrail-induced cirrus and carbon dioxide. The approximate area influenced by the CCC (Figures 6 and 13) is estimated to be 23,000 km^2, and the radiative forcing $\Delta F_{\text{net\_TOA}}$ is assumed to be +10 W m^{-2} during daylight hours and +30 W m^{-2} during nighttime hours (Figure 13), acting from approximately 0900 to 0300 UTC the next day. We assume that sunlight hours extend from 0600 to 1800 UTC, then the SW and LW effects act together for the first 9 h and LW effects act alone for the remaining 9 h so that the local mean forcing is about 20 W m^{-2} for an 18 h period or 15 W m^{-2} for a 24 h period. This is equivalent to a global mean radiative forcing in the 24 h period of $\sim$0.7 mW m^{-2}. Hence, this single event may have caused a forcing which is an appreciable fraction (7%) of the diurnally averaged global-mean persistent contrail forcing (10 mW m^{-2}). Alternatively, when averaged over a year, the event generated by the AWACS aircraft contributes approximately 2 μW m^{-2} or 0.02% of the annual global mean radiative forcing from persistent contrails from the entire fleet of civil aircraft: 5000 such events per year would need to occur to generate a global annual mean radiative forcing of 10 mW m^{-2}.

[43] We can also estimate the distance flown by the AWACS aircraft (10 complete circles of 40 km diameter $\sim$1250 km) and the distance flown by the entire civil aviation fleet (3.3 $\times$ 10^{10} km, on an annual basis [*Eyers et al.*, 2004]). If we consider the best estimate for the global mean radiative forcing due to persistent contrails to be 10 mW m^{-2}, then the entire civil fleet contributes a radiative forcing per kilometer due to persistent contrail formation of around 3 $\times$ 10^{-13} W m^{-2} km^{-1}. The AWACS aircraft exerts a global annual mean forcing of approximately 2 μW m^{-2} for a distance traveled of 1250 km leading to a radiative forcing per kilometer due to contrail-induced cirrus of 1.6 $\times$ 10^{-9} W m^{-2} km^{-1}; this is over 5000 times greater indicating that aviation operations that generate contrail-induced cirrus could exert a disproportionately high radiative forcing and hence warming of the climate system.

[44] Of course, it is possible that natural cirrus could have been generated in the absence of the AWACS and other aircraft operations. The very high supersaturation with respect to ice in this specific case study mean that other meteorological "triggers" causing the downstream evolution of natural cirrus cannot be ruled out. To establish that natural cirrus would not have formed in the absence of the aircraft operations would require very accurate modeling of processes that are only crudely represented in current numerical weather prediction models.

[45] These calculations emphasize the importance of obtaining a reliable estimate of the global role of contrail-induced cirrus and of understanding the extent to which they add to natural cirrus cover. In this particular instance, because of the distinct pattern of the original contrails, it has been possible to follow, with some degree of confidence, the causal sequence from contrails to contrail-induced cirrus. In normal circumstances this would not be possible, and it will be important to ascertain whether the sequence of events, and the size of the effect, that we have inferred is a regular occurrence.

[46] This work indicates that a confident assessment of the total effect of aviation on climate, and the efficacy of possible mitigation options (for example, changing flight routing or altitudes to avoid contrail formation, with the possibility that CO$_2$ which has a radically longer lifetime will increase as a result) is heavily dependent on reducing the uncertainty in the size of the contrail-induced radiative forcing.

References

Allan, R. P., A. Slingo, S. F. Milton, and M. A. Brooks (2007), Evaluation of the Met Office global forecast model using Geostationary Earth Radiation Budget (GERB) data, *Q. J. R. Meteorol. Soc.*, *133*, 1993–2010.

Burkhardt, U., and B. Kärcher (2009), Process-based simulation of contrail cirrus in a global climate model, *J. Geophys. Res.*, *114*, D16201, doi:10.1029/2008JD011491.

Clerbaux, N., S. Dewitte, C. Bertrand, D. Caprion, B. De Paepe, L. Gonzalez, A. Ipe, and J. E. Russell (2008a), Unfiltering of the Geostationary Earth Radiation Budget (GERB) Data. Part II: Longwave radiation, *J. Atmos. Oceanic Technol.*, *25*, 1106–1117, doi:10.1175/2008JTECHA1002.1.

Clerbaux, N., S. Dewitte, C. Bertrand, D. Caprion, B. De Paepe, L. Gonzalez, A. Ipe, J. E. Russell, and H. Brindley (2008b), Unfiltering of the Geostationary Earth Radiation Budget (GERB) Data. Part I: Short-wave Radiation, *J. Atmos. Oceanic Technol.*, *25*, 1087–1105, doi:10.1175/2007JTECHA1001.1.

Cusack, S., A. Slingo, J. M. Edwards, and M. Wild (1998), The radiative impact of a simple aerosol climatology on the Hadley Centre GCM, *Q. J. R. Meteorol. Soc.*, *124*, 2517–2526.

Edwards, J. M., and A. Slingo (1996), Studies with a flexible new radiation code: I. Choosing a configuration for a large scale model, *Q. J. R. Meteorol. Soc.*, *122*, 689–720, doi:10.1002/qj.49712253107.

Essery, R. L. H., M. J. Best, R. A. Betts, P. M. Cox, and C. M. Taylor (2003), Explicit representation of subgrid heterogeneity in a GCM land surface scheme, *J. Hydrometeorol.*, *4*, 530–543, doi:10.1175/1525-7541(2003)004<0530:EROSHI>2.0.CO;2.

Eyers, C., P. Norman, J. Middel, M. Plohr, S. Michot, K. Atkinson, and R. Christou (2004), AERO2k global aviation emissions inventories for 2002 and 2025, technical report, QinetiQ Ltd., Farnborough, U. K.

Fahey, D., U. Schumann, S. Ackerman, P. Artaxo, O. Boucher, M. Y. Danilin, B. Kärcher, P. Minnis, T. Nakajima, and O. B. Toon (1999), Aviation-produced aerosols and cloudiness, in *Aviation and the Global Atmosphere*, edited by J. E. Penner et al., pp. 65–120, Cambridge Univ. Press, Cambridge, U. K.

Forster, P., et al. (2007), Changes in atmospheric constituents and in radiative forcing, in *Climate Change 2007: The Physical Science Basis: Contribution of Working Group I to the Fourth Assessment Report of the Intergovernmental Panel on Climate Change*, edited by S. Solomon et al., pp. 129–234, Cambridge Univ. Press, Cambridge, U. K.

Gayet, J.-F., J. Ovarlez, V. Shcherbakov, J. Ström, U. Schumann, A. Minikin, F. Auriol, A. Petzold, and M. Monier (2004), Cirrus cloud microphysical and optical properties at southern and northern midlatitudes during the INCA experiment, *J. Geophys. Res.*, *109*, D20206, doi:10.1029/2004JD004803.

Haywood, J. M., R. P. Allan, I. Culverwell, A. Slingo, S. Milton, J. Edwards, and N. Clerbaux (2005), Can desert dust explain the outgoing longwave radiation anomaly over the Sahara during July 2003?, *J. Geophys. Res.*, *110*, D05105, doi:10.1029/2004JD005232.

Intergovernmental Panel on Climate Change (IPCC) (1999), *Special Report on Aviation and the Global Atmosphere*, edited by J. E. Penner et al., Cambridge Univ. Press, Cambridge, U. K.

Intergovernmental Panel on Climate Change (IPCC) (2007), *Climate Change 2007: The Physical Science Basis: Contribution of Working Group I to the Fourth Assessment Report of the Intergovernmental Panel on Climate Change*, edited by S. Solomon et al., Cambridge Univ. Press, Cambridge, U. K.

Jones, A. R. (2004), Atmospheric dispersion modelling at the Met Office, *Weather*, *59*, 311–316, doi:10.1256/wea.106.04.

Kärcher, B., and P. Spichtinger (2009), Cloud-controlling factors of cirrus, in *Clouds in the Perturbed Climate System: Their Relationship to Energy Balance, Atmospheric Dynamics, and Precipitation, Strüngmann Forum Rep. 2*, edited by J. Heintzenberg and R. J. Charlson, pp. 235–267, MIT Press, Cambridge, Mass.

Lacis, A. A., and J. E. Hansen (1974), A parameterization for the absorption of solar radiation in the Earth's atmosphere, *J. Atmos. Sci.*, *31*, 118–131, doi:10.1175/1520-0469(1974)031<0118:APFTAO>2.0.CO;2.

Lean, H. W., P. A. Clark, M. Dixon, N. M. Roberts, A. Fitch, R. Forbes, and C. Halliwell (2008), Characteristics of high-resolution versions of the Met Office unified model for forecasting convection over the United Kingdom, *Mon. Weather Rev.*, *136*, 3408–3424, doi:10.1175/2008MWR2332.1.

Lee, D. S., D. W. Fahey, P. M. Forster, P. J. Newton, L. L. Lim, B. Owen, and R. Sausen (2009), Aviation and global climate change in the 21st century, *Atmos. Environ.*, *43*, 3520–3537.

Mannstein, H., and U. Schumann (2005), Aircraft induced contrail cirrus over Europe, *Meteorol. Z.*, *14*, 549–554, doi:10.1127/0941-2948/2005/0058.

Mannstein, H., and U. Schumann (2007), Corrigendum, *Meteorol. Z.*, *16*, 131–132, doi:10.1127/0941-2948/2007/0178.

Minnis, P., D. F. Young, D. P. Garber, L. Nguyen, W. L. Smith, and R. Palikonda (1998), Transformation of contrails into cirrus during SUCCESS, *Geophys. Res. Lett.*, *25*(8), 1157–1160, doi:10.1029/97GL03314.

Minnis, P., J. K. Ayers, R. Palikonda, and D. Phan (2004), Contrails, cirrus trends, and climate, *J. Clim.*, *17*, 1671–1685, doi:10.1175/1520-0442(2004)017<1671:CCTAC>2.0.CO;2.

Myhre, G., and F. Stordal (2001), On the tradeoff of the solar and thermal infrared radiative impact of contrails, *Geophys. Res. Lett.*, *28*, 3119–3122, doi:10.1029/2001GL013193.

Nakajima, T., and M. D. King (1990), Determination of the optical thickness and effective particle radius of clouds from reflected solar radiation measurements. Part I: Theory, *J. Atmos. Sci.*, *47*, 1878–1893, doi:10.1175/1520-0469(1990)047<1878:DOTOTA>2.0.CO;2.

Newman, S. M., F. Hilton, and A. Collard (2008), Identification of biases in the modelling of high peaking water vapour channels from IASI, paper presented at 16th International TOVS Study Conference, Int. TOVS Working Group, Angra dos Reis, Brazil, 6–13 May.

Prather, M., R. Sausen, A. S. Grossman, J. M. Haywood, D. Rind, and B. H. Subbaraya (1999), Potential climate change from aviation, in *Aviation and the Global Atmosphere*, edited by J. E. Penner et al., pp. 185–215, Cambridge Univ. Press, Cambridge, U. K.

Rädel, G., and K. P. Shine (2007), Evaluation of the use of radiosonde humidity data to predict the occurrence of persistent contrails, *Q. J. R. Meteorol. Soc.*, *133*, 1413–1423, doi:10.1002/qj.128.

Rädel, G., and K. P. Shine (2008), Influence of aircraft cruise altitudes on radiative forcing by persistent contrails, *J. Geophys. Res.*, *113*, D07105, doi:10.1029/2007JD009117.

Rodgers, C. D. (1967), The radiative heat budget of the troposphere and lower stratosphere, *Rep. A2*, Planet. Circ. Proj., Dept. of Meteorol., Mass. Inst. Technol., Cambridge.

Ryall, D. B., and R. H. Maryon (1998), Validation of the UK Met Office's name model against the ETEX dataset, *Atmos. Environ.*, *32*, 4265–4276, doi:10.1016/S1352-2310(98)00177-0.

Sausen, R., et al. (2005), Aviation radiative forcing in 2000: An update on IPCC (1999), *Meteorol. Z.*, *14*, 555–561, doi:10.1127/0941-2948/2005/0049.

Stordal, F., G. Myhre, E. J. G. Stordal, W. B. Rossow, D. S. Lee, D. W. Arlander, and T. Svendby (2005), Is there a trend in cirrus cloud cover due to aircraft traffic?, *Atmos. Chem. Phys.*, *5*, 2155–2162.

Stuber, N., P. Forster, G. Rädel, and K. P. Shine (2006), The importance of the diurnal and annual cycle of air traffic for contrail radiative forcing, *Nature*, *441*, 864–867, doi:10.1038/nature04877.

Vömel, H., H. Selkirk, L. Miloshevich, J. Valverde-Canossa, J. Valdès, E. Kyrö, R. Kivi, W. Stolz, G. Peng, and J. A. Diaz (2007), Radiation dry bias of the Vaisala RS92 humidity sensor, *J. Atmos. Oceanic Technol.*, *24*, 953–963, doi:10.1175/JTECH2019.1.

———————————

R. P. Allan, ESSC, University of Reading, 3 Earley Gate, Whiteknights Road, Reading RG6 6AL, UK.

J. Bornemann, P. N. Francis, J. M. Haywood, S. Milton, and R. Thorpe, Forecasting Research and Development, Met Office, Cordouan 2, FitzRoy Road, Exeter EX1 3PB, UK. (jim.haywood@metoffice.gov.uk)

P. M. Forster and A. Rap, Department of Environmental Science, University of Leeds, Leeds LS2 9JT, UK.

G. Rädel and K. P. Shine, Department of Meteorology, University of Reading, Earley Gate, PO Box 243, Reading RG6 6BB, UK.